Periodic Obstacles Regulate Membrane Tension Propagation to Enable Localized Mechanotransduction

Frederic Català-Castro[1,*], **Mayte Bonilla-Quintana**[2,*], **Neus Sanfeliu-Cerdán**[1], **Padmini Rangamani**[2,3,#], **Michael Krieg**[1,#]

[1] ICFO - Institut de Ciències Fotòniques, Castelldefels, The Barcelona Institute of Science and Technology, Barcelona, Spain
[2] Department of Mechanical and Aerospace Engineering, University of California San Diego, La Jolla, USA.
[3] Department of Pharmacology, School of Medicine, University of California San Diego, La Jolla, USA.
[*] shared first author
[#] correspondence to: prangamani@health.ucsd.edu; michael.krieg@icfo.eu

Abstract

Forces applied to cellular membranes lead to transient membrane tension gradients. The manner in which membrane tension propagates away from the stimulus into the membrane reservoir has emerged as a key property in cellular adaptation, mechanotransduction, and thus organismal physiology. However, it remains unclear whether tension propagation in membranes is actively regulated or is a passive property and how it depends on the cell type. Here, we combined membrane nanorheology with time-shared optical traps and mathematical modeling to investigate plasma membrane tension propagation in cultured *Caenorhabditis elegans* mechanosensory neurons using a dual tether extrusion assay. Our results showed that, surprisingly, the propagation of tension was restricted to 30 µm in the neurites and traveled quickly, at speeds exceeding 120 µm/s. Although membrane lipid properties had minimal impact, tension propagation strongly relied on the intact actin and microtubule cytoskeleton. In particular, the organization of the α/β -spectrin network and the MEC-2 stomatin condensates acted as barriers, limiting the spread of tension. A biophysical model for tension propagation suggests that obstacle density and arrangement play a key role in controlling the propagation of mechanical information. Our findings suggest that restricting membrane tension propagation in space and time enables precise localized signaling. This localization may facilitate the recruitment of mechanosensitive ion channels and allow a single neuron to process mechanical signals in multiple distinct domains, thus expanding its computational capacity.

1 Introduction

The transmission of mechanical information through the cytoskeleton, organelles, and plasma membrane is vital for the organization of cells and mechanotransduction[1, 2]. Plasma membrane mechanics plays an important role in the cellular response to external forces and determines cell shape [3], signaling [4], and metabolism [5]. Mechanical properties are characterized by an in-plane membrane elasticity, an elastic restoring force that resists bending deformations, a viscosity that resists flow and, originating from its coupling to the cell cortex, an effective membrane tension [6]. Furthermore, it has been extensively reported that local tension gradients, due to a large membrane reservoir or the fluid character of

the lipid bilayer, rapidly relax in metazoan cells [7, 8, 9, 10, 11, 12] but may be heterogeneous along the contour of the cell [13, 14, 15, 16]. Thus, the existence of such a lipid reservoir leads to the fact that the membrane cannot support and store mechanical stresses on times greater than their viscous relaxation timescales, leading to a constant membrane tension [7]. Due to this, it is believed that a local increase in tension generated by an application of local forces (due to an external tether extrusion [7] or an internal actin protrusion [17]) is rapidly propagated across the entire membrane surface. This idea has placed membrane tension as an effective mediator of communication between mechanical events occurring at different locations along the membrane[18, 17]. However, the specific details of the propagation of membrane tension appear to be system specific [15, 18, 10, 19] For example, these views were recently challenged by the observation that membrane tension does not propagate in tissue culture cells, suggesting that the increased tension gradient remains locally confined to regions around the neck of the tether and does not relax for many minutes [15]. Likewise, in bacterial cells, the tension generated during tether pull did not relax, indicating that the tension of the resting membrane is globally regulated and close to the lytic tension [20]. However, in axons of cultured neurons[18, 19], tension was shown to propagate many tens of micrometers.

This raises questions about how tension propagation is regulated along the membrane and the cellular adaptation mechanism to an external force. To provide insight into these questions, we established optical tweezer-based membrane nanorheology with a single, time-shared laser source[21, 22] to study membrane tension propagation mechanics between a pair of lipid nanotubes extruded from a single axon. We used the well-studied touch receptor neurons of *Caenorhabditis elegans* as a biophysical model for tension propagation in axons. This model system has gained interest in the mechanophysiological regulation of animal behavior[23, 24, 25]. These neurons are important for the animal's response to external forces. Although the exact mechanism of mechanotransduction is still not defined, genes affecting mechanoresponses are known and encode proteins of the extracellular matrix[26], microtubules[27], integral and peripheral membrane proteins[28, 29] and the cortical cytoskeleton[30], but also the membrane itself[31].

To understand the link between these cellular elements and tension propagation, we combine our experimental results with a theoretical model proposed by [18, 15], in which tension propagation is associated with membrane lipid flow, but hindered by cytoskeleton-bound transmembrane proteins. The basic principle of our model is the same as those proposed before [18, 15], which is based on Brinkman flow [32] and we conduct three-dimensional simulations using finite-element methods to compare the effect of different parameters on tension propagation. Our results suggest that membrane tension is locally confined and, accordingly, we reveal that tension propagation into the axon is limited by obstacles, such as membrane-bound biomolecular condensates. Because we find that the extent of propagation differs between proprioceptive and touch mechanoreceptors that respond to different modalities, we propose that propagation speed and magnitude is an intrinsic property and under tight genetic control.

2 Results and Discussion:

The active trap To study how cell membrane mechanics enables plasma membrane tension propagation, we began our investigation with the classical tether extrusion experiment[33]. Similarly to our previous approach with mechanosensitive proprioceptors[10], we used an optically trapped microsphere as a force probe and formed a contact between the probe and the membrane of isolated touch receptor neurons of *C. elegans*. Upon successful nonspecific attachment, rapid retraction of the microsphere leads to an increase in force on the trapped bead, indicating the extrusion of a lipid nanotube (Suppl.

Fig. 1a). After reaching a predefined distance from the axon, we stopped the movement of the trap and held the probe at a constant position. Immediately, the tether force rapidly decayed to a static value, independent of the initial extrusion velocity and, therefore, independent of membrane viscosity (Suppl. Fig. 1a), similar to what was observed before[33]. As noted previously, a higher retraction velocity caused an increased force on the microsphere[10], due to the finite viscosity and the resulting resistance of the membrane to flow into the tether (Suppl. Fig. 1b) and [34, 35]). This viscosity-dominated peak increased with velocity up to 120 pN and was suggestive of the maximum tension gradient of up to 1 mN/m generated during pull-out (Suppl. Fig. 1)b,c). As the rapid increase in tension during the tether pullout is not due to fluid drag of the probe with the surrounding medium, we reasoned that limited lipid flow into the tether caused this striking tension gradient.

Indeed, and especially at high extrusion velocities, we frequently observed spherical instabilities that originated close to the tether neck and traveled toward the microsphere (Video 2, Suppl. Fig. 1) d). Such dynamics is inherent in Rayleigh-Plateau instabilities (RPI, [36]). An RPI is a mechanical instability driven by surface tension and leads to the breakup of a cylindrical liquid-like column into droplet-like beads on a string[37]. More specifically, the RPI appears when fluid cylinders are subjected to extensional flow under mass conservation (e.g. no lipid transport into the tether); thus extension is faster than the lipid diffusion. Interestingly and in contrast to previous observations[18], our RPI was confined to the tether and never visually propagated to the axonal membrane, indicating that the increase in membrane tension was locally confined and hardly propagated into the axon (Suppl. Fig. 1) d). From this we conclude that there exists a strong tension gradient inside the tether, which does not, or incompletely, propagate into the axon.

The active and the passive trap To gain insight into the mechanism of tension propagation in neurons, we directly measured the extent of tension propagation along the axon to a point perturbation. To do so, we established an optical trapping experiment to simultaneously extrude two membrane tethers with a single, time-shared laser source (Fig. 1a, Suppl. Fig. 2). Akin to our previous time-shared optical tweezers microrheology scheme (TimSOM, [22]), we split a single laser source at 25 kHz to generate two traps that can be moved independently in 2D (Fig. 1a, Suppl. Fig. 2, Methods). Using these two effectively-simultaneous optical traps, we extruded a single membrane tether with each of the two traps that were placed in close proximity to each other (Fig. 1 a). Then, we actively pulled from the tether in trap 1, while measuring the response in the static tether, held with trap 2 (Fig. 1b). We alternated this procedure for trap 1 and trap 2 and repeated the extrusion protocol for dual tether distances (DTD) up to 40 µm (Fig. 1c, Video 1).

Contrary to the active trap, the passive trap displayed rich behavior. At close separations from the active trap (directly opposite to the active trap), we observed a strong reduction in the propagated peak force (Fig. 1c). Only ≈40% of the force of the active trap reached the passive trap, even at distances less than 1 µm. However, the force transmission velocity from the active to the passive tether was very rapid and, contrary to previous work[15], exceeded ≈ 100 µm/s (Suppl. Fig. S1e). With increasing distance from the active tether, the peak of the passive trap decreased substantially (Fig. 1 d) until it seemed to disappear. At > 20 µm tether separation, the peak was completely buffered. Instead, we observed a slow and steady (≈ second scale) increase to a plateau value, suggesting that the membrane behaves as a low-pass filter for mechanical signal transmission - only the slow components get propagated up to 40 µm (Fig. 1b).

We then sought to understand whether tension propagation is different in mechanoreceptor neurons

with different functions and turned to DVA proprioceptors. The DVA neuron differs from TRNs in that it contains a single axon, which senses local changes in body bending to coordinate body curvature[38, 10]. We have previously shown that local forces applied by an optical trap initiate local calcium dynamics in response to force relaxation and suppress calcium activity with increasing tension (through mechanosensitive TRP and K2P ion channels)[10]. We thus speculated that mechanical stresses compartmentalize the axon into dynamic active zones. One requirement of this model is that the spread of mechanical information is limited within the axonal membrane. By applying our dual tether assay, we found that the static tether force is higher compared to TRNs (Fig. 1d ii; Cohen's D = 0.4, p = 0.002) and that the tension propagated less and remained more confined in DVA (Fig. 1d i) compared to the measurements in TRNs (Fig. 1, 12.5 vs 9.8 µm). Together, this indicates that membrane tension propagated further in TRNs. More general, our data show that the extent of membrane tension propagation is cell-type specific, which motivated us to dissect the molecular and mechanical mechanism of tension propagation in neurons.

2.1 Membrane tension propagation is restricted by membrane obstacles

Following recent attempts to describe tension propagation quantitatively[15], we assumed that membrane lipid flow transmits local changes in tension and that cytoskeleton-bound transmembrane proteins, such as cell adhesion molecules, ion channels, and membrane-cortex cross-linkers, act as obstacles impeding membrane flow (see Methods). These dynamics are described by

$$\frac{E_0}{\eta}\nabla^2\sigma = \left(-\nabla^2 + \frac{1}{k}\right)\frac{\partial\sigma}{\partial t}, \tag{1}$$

where σ is the membrane tension, E_0 represents the effective area expansion modulus of the cell membrane, η is the two-dimensional membrane viscosity, and k is the Darcy permeability of the obstacles (Fig. 2a). We use a cylinder as an idealized geometry for a segment of the axon, and the tethers are represented by attached thinner cylinders (Fig. 2a). As in [15, 18], we define the permeability $k = a^2 f(\phi)$ by the obstacle area a and a function of the obstacle density ϕ, $f(\phi) = -(1 + \ln(\phi))/(8\phi)$. Thus, increased permeability results from a reduced number of obstacles covering the same area, as well as an increase in obstacle size, which can occur due to molecule clustering (Fig. 2b).

From Eq. 1, we observed that tension propagation is governed by the parameters E_0, η, and k. Hence, we examined the effect of changing these parameters in the tension propagation using finite element simulations in a cylindrical geometry (see Materials and Methods for details). When permeability k is high, there are less and/or smaller obstacles in the membrane that allow it to flow more freely. Consequently, the propagation of tension increases as the permeability increases (k, Fig. 2c). Our model also incorporates membrane elasticity and we asked to what extent E_m affects tension propagation. We found that the more elastic the membrane, the greater the tension at the tether, which increases the extent of tension propagation along the axon (Suppl. Fig. 3a). Lastly, we hypothesized that a higher viscosity hinders the lipid flow of the membrane and, hence, localizes the tension propagation to a smaller region. Indeed, when the viscosity η increases, we observed a decrease in tension propagation (Suppl. Fig. 3b). Together, our simulations suggest a striking dependence of tension propagation on membrane in plane elasticity, viscosity, and obstacle density.

Recent studies have shown that ion channels are organized in a periodic arrangement along the axon[39] and dendrites[40]. Our initial model assumes that obstacles are randomly and homogeneously

placed in neurites, which may not reflect the physiological organization in neurons. This periodicity is governed by the actin-spectrin cytoskeleton, in which the spectrin tetramers expand $\approx$ 190 nm and connect adjacent actin rings (Fig. 2d). We modeled this periodicity along the axon assuming that 2/3 of the axonal membrane is covered by channels and 1/3 by smaller obstacles attached to the actin rings (Fig. 2e). We proposed that permeability k in the zone related to actin rings is higher $k_+ = 1.5k$ than in the zones covered by channels $k_- = (3k - k_+)/2$ (Fig. 2e). We varied the parameters and observed that tension propagated less in the periodic control case, i.e. using k from the homogeneous control case to calculate k_+ and k_-, than in the homogeneous control case (Fig. 2f). In all cases, the ratio of the passive to the active tension peak is higher compared to the random obstacle arrangement. This indicates that a periodic arrangement leads to more localized tension and less propagation along the axon. Indeed, our parameter sweep confirmed this assessment even though the parameters show the same tendency as in the homogeneous case (Fig. 2f; Suppl. Fig. 3 c, d, the periodic control case is gray). Together, tension propagation was hindered when obstacles are organized into periodic clusters.

We note that the parameters in the model cannot be directly assigned to individual cell membrane properties as a result of the complex nature of membrane-cortex interactions. Thus, we simulated the model changing two parameters simultaneously. Fig. 2g-i shows a cooperative effect in the propagation of tension when these parameters are changed. In Fig. 2g, we observe that the degree of tension propagation depends on the ratio η/E_0. Note that in Eq. 1, this ratio gives the time scale of the dynamics. In summary, we detected a stronger cooperative relationship between the parameters k and η and that the periodic arrangement of the obstacles affected the propagation of tension in silico.

2.2 Lipid saturation has little influence on tension propagation

Through AFM-based tether pulling experiments[35] from the cell body of touch receptor neurons, we have previously shown that lipid saturation modifies the viscous properties of the membrane but not the steady-state tension[31]. Therefore, we ask whether lipid saturation and osmotic effects influence tension propagation along the neurite. *fat-3* mutant neurons with defects in polyunsaturated fatty acid synthesis (PUFA) [41, 31] did not have a discernible effect (Fig. 3 a, b). However, because our tissue culture medium contained 10% fetal bovine serum, the effect of *fat-3* may be partially confounded by the PUFAs in the medium[42]. Recently, intracellular pressure was shown to influence the rate at which tension propagated along the membrane in HEK293T cell cultures[43]. We also observed that the application of a hypoosmotic shock significantly increased the tether force (Cohen's D=0.14; p=0.0008). However, we detected only a modest difference in tension propagation compared to wildtype (Fig. 3; α= 12 vs 14µm). Together, these data show that tension propagation is surprisingly robust to subtle changes in the composition of the lipid bilayer and increases with intracellular osmotic pressure. It further suggests that tension propagation may be dominated by obstacles in the membrane and the cytoskeleton.

2.3 The scale of tension propagation is modulated by the cytoskeleton

In our simulations, we treated the membrane and the underlying cytoskeleton as a composite material and assumed that changes in the cytoskeleton affect membrane permeability. This is because transmembrane proteins, which connect to the actin cytoskeleton, can act as obstacles to the flow of lipids in the membrane, as suggested in previous work [44]. Therefore, we measured tension propagation and static tension in four different treatments with Latrunculin A (LatA), an agent that sequesters actin monomers and is known to interfere with actin polymerization[45], and also Cytochalasin D (CytoD), a drug known

to depolymerize dynamic actin filaments[46]. At low concentrations of LatA (delivered at 0.5-10 μM acutely, 30 min incubation time), we did not observe an effect on membrane tension (Fig. 4 a) or on tension propagation (Suppl. Figs. 4 and 5). This is consistent with earlier studies showing that low concentrations of LatA did not interfere with actin ring disassembly in *Drosophila* neurons[47] and does not disrupt stable actin filaments. Intriguingly, the acute application of 1μM LatA, but also 2 μM of acute CytoD delivery led to a seemingly surprising increase in static membrane tension (Fig. 4a). Interestingly, these acute treatments with low concentrations of LatA and CytoD led to an increase in tension propagation (Fig. 4 and Fig. 4b), suggesting that a higher membrane permeability facilitates flow. However, after chronic incubation of neurons (1 μM LatA or 2 μM CytoD over night), we observed a significant reduction in static membrane tension (LatA: Cohen's D=0.48; p=0.0001; CytoD, p=0.0002; Fig. 4a). The propagation of membrane tension was also differently affected by different drug concentrations. We found that chronic application of high concentrations of LatA and CytoD resulted in very limited tension propagation (ctrl vs. LatA vs. CytoD; 12 vs 9.3 vs 8.8μm, Fig. 4b). In general, this is consistent with our previous work and that of others, showing that actin perturbation in neurons is more sensitive to cytochalasin D (CytoD) but not to acute incubation with Latrunculin A (LatA)[30, 47].

We reasoned that different concentrations of latrunculin and cytochalasin perturb different populations of actin filaments, as previously observed in MDCK cells[48]. This could be understood in transient decoupling of the cortex membrane (increase in k) with low concentrations of drugs, followed by a decrease in membrane elasticity (decrease in E_m) in chronic drug application. To understand how propagation is subject to the mechanical properties of the membrane-cytoskeleton composite, we turned to our model and simulated different conditions of E_m and k. Indeed, a decrease in membrane elasticity leads to a decrease in propagated tension, where an increase in k led to increased tension propagation (Fig. 4 and Fig. 4c).

Having shown that actin has a substantial effect on axonal membrane mechanics, we next asked if tension propagation in the membrane is modulated by microtubules. Indeed, a prominent hallmark of neurons in general and *C. elegans* TRNs in particular are their thick bundles of acetylated microtubules[49, 50]. We then extruded tethers from *mec-12(e1607)* mutants lacking discernible MEC-12 α-tubulin expression [51]), and we found that the absence of microtubules only weakly affected static membrane tension (Cohen's D=0.14; p=0.035). However, nocodazole treatment of neurons led to a significant and strong increase in static tension (Fig. 4d; Cohen's D=0.44), which was similar to the cells acutely treated with cytochalasin D. One possible explanation is that highly abundant post-translational acetylation of MEC-12 α tubulin confers sensitivity to nocodazole[52] and leads to unexpected stabilization and membrane coupling, which is visible as increased resistance to tether extrusion and static membrane tension (Fig. 4d). In fact, MTs are coupled to the membrane cortex through a ternary complex composed of ankyrin UNC-44, crmp UNC-33 and unc-119 UNC119, which bind the bundles of MTs to the spectrin cytoskeleton, and share the same ≈200 nm periodicity [53]. Intriguingly, the loss of microtubules in both conditions, the *mec-12* mutant and the treatment with nocodazole, was accompanied by a significantly decreased tension propagation compared to ctrl (8.1 vs 12.3 μm, Fig. 4e,f). Together, this shows that the microtubule cytoskeleton supports membrane tension propagation along the axons.

2.4 The periodicity of the actin/spectrin cytoskeleton sets limits on tension propagation

It is well established that the spectrin cytoskeleton coordinates many transmembrane proteins (ion channels, adhesion receptors, dystroglycans, band 4 proteins) and also binds to the membrane itself[54]. Thus, it is plausible that the periodic spectrin cytoskeleton establishes a barrier that impedes free tension propagation by establishing periodic obstacles. Indeed, when we simulated periodically arranged obstacles, rather than randomly distributed clusters, tension propagated less (Fig. 2f). In other words, the loss of periodicity leads to an increase in tension propagation.

UNC-70 is the sole β-spectrin homolog in *C. elegans* neurons and forms a complex with α-spectrin. In C elegans, similar to the neuronal cytoskeleton in mammals, both components form a characteristic periodicity of 190 nm and bind to both the actin cytoskeleton and the membrane in vitro and in vivo[25, 39, 40]. This periodicity is more variable in intact animals[55] and completely lost in the absence of functional UNC-70, as visualized using α-spectrin as a proxy for the spectrin network (Fig. 4g and [25]). Similarly to the model predictions (Fig. 4 h), the propagation of tension along the axon of *unc-70* null mutants was substantially increased (Fig. 4i), suggesting that the loss of β-spectrin leads to discretely clustered domains of transmembrane proteins[56] and concomitant increase in permeability. However, our model does not rule out other factors, such as transmembrane receptor endocytosis, which may further lead to an increase in tension propagation in the spectrin mutant[57]. Together, our results from the experiments and the modeling suggest that periodic membrane obstacles and components of the cytoskeleton focus on membrane tension propagation. Our observations suggest that the distinct periodicity of the actin/spectrin network is a mediator of the organization of transmembrane and membrane-associated proteins and thus the propagation of tension in neurons.

2.5 Stomatin MEC-2 condensation at the membrane impedes tension propagation

Lastly, we tested if obstacles in the membrane can indeed influence membrane tension propagation. We have previously shown that MEC-2 stomatin, a protein associated with stiffened membrane domains[58], forms biomolecular condensates proximal to the inner leaflet of the plasma membrane[28]. In vivo and in vitro, an MEC-2 condensate is periodically arranged and can be found every 2-4 µm and 1-2 µm (Fig. 5), respectively. To understand whether condensation of MEC-2 on the plasma membrane influences tension propagation, we performed tether extrusion in *mec-2* knockout animals. Interestingly, we observed substantially larger tension propagation in the neurite of *mec-2* mutants (ctrl vs. *mec-2*; 12.3 vs 18.5 µm), even though the static membrane tension is not different (Fig. 5a; Cohen's D=0.07). Thus, we ask whether obstacles like MEC-2 impede tension propagation in our model. Indeed, as shown above, our simulations predicted that membranes with a higher permeability would enhance tension propagation (Fig. 5c). Therefore, removing MEC-2, which binds to the inner leaflet of the plasma membrane through its cholesterol binding ability, reduces obstacle density and increases k, also increases tension propagation.

MEC-2 stomatin is a cholesterol-binding protein, and the disruption of its cholesterol-binding ability alters the regulation of the ion channel [59, 60]. The addition of cholesterol to biomembranes has been shown to increase the membrane expansion modulus (E_m), effectively making the membranes stiffer [61]. This prompted us to investigate how cholesterol depletion affects tension propagation in cultured neurons. As shown above, stiffer membranes propagate tension better (Suppl. Fig. 3d). However, ex-

periments revealed the opposite: treating neurons with cyclodextrin to sequester cholesterol significantly increased tension propagation (control vs. treated: 12 µm vs. 20.5 µm), similar to the effects observed with genetic disruption of *mec-2* (Fig. 5d). This surprising increase in tension propagation is inconsistent with the idea of softer membranes alone (Fig. 2g). Instead, we propose that it results from a reduction in obstacle density and clustering within the membrane, as seen in both *mec-2* mutants and cholesterol-depleted neurons. Indeed, mutant MEC-2(P134S) that cannot bind cholesterol was shown to disrupt proper localization and organization of MEC-2 in the membrane of touch receptor neurons[59]. Collectively, these data suggest that MEC-2 condensates act as an obstacle, interacting with cholesterol in the membrane to limit the propagation of membrane tension.

3 Conclusion

Using *C. elegans* as a model for mechanotransduction and neuroscience, we dissected the molecular signature of mechanical stress propagation along the neuronal membrane of sensory neurites in neurons responsible for the sense of touch and proprioception. With an optical-tweezer-based membrane tube extrusion assay, we found that, unlike our previous observations of tubes extruded from zebrafish progenitor cells [35, 3] or the soma of cultured TRN [30, 31], the tension did not remain constant during the extrusion protocol, suggesting a limited membrane reservoir that is unable to buffer tension gradients in axons [7]. We found that steep gradients of membrane tension propagate fast (>120 µm/s) but to a limited distance (< 12 µm), which depended strongly on the cytoskeleton and barriers of the plasma membrane.

Our experimental results are consistent with the prediction from a biophysical model that a higher permeability (lower obstacle density) through membrane-cortex disruption leads to higher tension propagation. Interestingly, we observed that actin depolymerization with varying concentrations of LatA and CytoD had opposing effects on tension propagation. At acute delivery of low concentrations, propagation increased, presumably due to transient decoupling of membrane cortex binders, while at high and chronic treatments, tension propagation was reduced. Based on our simulations, we speculate that chronic actin depolymerization decreased effective membrane elasticity due to disruption of caveolae and other membrane domains, essentially increasing the available membrane lipid reservoir[62, 63].

We propose that mechanical signals must remain confined to be locally processed, much like local computations at synapses. Why is restricted propagation advantageous? It enhances the cell's ability to detect precise, localized mechanical cues, enabling parallel processing of simultaneous stimuli and targeted responses. Allowing unrestricted propagation of mechanical information along the axon could blur receptive field boundaries, introducing disruptive background noise. Our data showing that tension propagation is different in touch receptors and proprioceptors suggests differential expression of membrane obstacles such as cortex crosslinkers. Recent single cell gene expression data sets show that DVA expresses 10 times more FRM-1 than TRNs[64], the major Band 4.1N ortholog of the FERM superfamily in *C. elegans* with roles in coupling various transmembrane receptors, channels, and adhesion molecules to actin / spectrin csk or stomatin proteins[65]. In fact, we have recently shown that FRM-1 is directly bound to UNC-70[55], but future work is necessary to refine the role of FRM-1 in this process.

Acknowledgements We would like to thank the NMSB laboratory for discussion, Felix Campelo (ICFO) for suggestions early in the work, Fred Hoerndli (Colorado State) for comments on the draft and

the *Caenorhabditis elegans* center (CGC, supported by the National Institutes of Health, P40 OD010440) for reagents.

Funding MK acknowledges financial support from the ERC (MechanoSystems, 715243), Human Frontiers Science Program (RGP021/2023), MCIN/ AEI/10.13039/501100011033/ FEDER "A way to make Europe" (PID2021-123812OB-I00, CNS2022-135906), "Severo Ochoa" program for Centres of Excellence in R&D (CEX2019-000910-S), from Fundació Privada Cellex, Fundació Mir-Puig, and from Generalitat de Catalunya through the CERCA and Research program. ICFO is the recipient of the Severo Ochoa Award of Excellence of MINECO (Government of Spain). P.R. was supported by 1RF1DA055668-01 and the Air Force Office of Scientific Research Grant FA9550-18-1-0051.

Conflict of interests The authors have no conflict of interest to declare.

Data availability All data are supplied as a source data sheet in the supplementary material of this manuscript.

Code availability All code is supplied through the gitlab account here.

4 Materials and Methods

4.1 *C. elegans* maintenance

Strains were maintained and manipulated under standard conditions [66]. Nematode strains were grown at 20°C on nematode growth medium (NGM) plates with OP50 bacteria and synchronized using the standard alkaline hypochlorite treatment method [67].

4.2 Primary cell culture and membrane extrusion

4.2.1 TRN primary cell culture

Primary cell culture was performed as described in [30, 10]. In short, gravid hermaphrodites that were previously grown onto large peptone enriched plates at 20-25°C were collected with milli-Q H2O and bleached following regular procedures [67]. Eggs were washed 3x with Egg Buffer (118 mM NaCl, 48 mM KCl, 2 mM $CaCl_2$, 2 mM $MgCl_2$, 25 mM HEPES, pH 7.3 and 340 mOsm) and separated through a final sucrose density gradient 30 % generated by 20 min centrifugation at 1200 rpm. Once the eggs were collected in a new vial, they were washed 2x with Egg Buffer and treated with chitinase (0.5 U/ml) for 40 min to digest their egg shell. The reaction was stopped with L15 medium. The embryos were then dissociated by passing the solution 10x through a 25G needle and filtered with a 5 µm Durapore filter (Millipore). Finally, cells were pelleted by 3 min centrifugation at 3200 rpm and resuspended with L15 medium. Cells were seeded at density $1.5 \cdot 10^6 mL^{-1}$ in optical trapping chambers (see below) and 1 ml of L15 medium was added after 3 h. They were cultured at 25°C and fresh medium was changed (1-2 mL) every day. All experiments were performed between two and four days after isolation. CO_2-independent L15 tissue culture medium supplemented with heat-inactivated bovine calf serum (10% v/v; FBS 11A

Capricorn Scientific), penicillin (10 mg mL-1), and streptomycin (100 units; L0022 Biowest) was used throughout the study[30].

The drugs were added 24-48 hours after isolation. Nocodazole (M1404, Sigma) was added at a final concentration of 1 µg/mL. Cytochalasin D (10 mM stock in DMSO, C2618, Sigma) was diluted 1:5000 in L15 medium to 2 µM final concentration. Latrunculin A (10 mM stock, L5163 Sigma) was diluted in L15 medium to a final concentration of 500 nM, 1 µM or 10 µM. Cyclodextrin (Methyl-β-cyclodextrin C4555, Sigma) was added to the final concentration of 3 or 7-10 mM. Cells were incubated with Nocodazole, Cyclodextrin or latrunculin A (acute) for 30 min, whereas Cytochalasin D and latrunculin A treatments were incubated overnight at 25 °C, followed by 3 washes of L15 with the corresponding drug. Hypoosmotic shocks were perfomed by diluting 1:2 L15 medium in water.

4.3 Optical micromanipulation and confocal microscopy

A multimodal platform was used that combined spinning-disk confocal microscopy and optical micromanipulation. Briefly, an optical micromanipulation unit (SensoCell, Impetux Optics) modulated with a pair of acoustooptic defletors (AOD) was coupled to the rear epifluorescence port of an inverted research microscope (Nikon Ti2 Eclipse). The optical traps were created at the focal plane of a 60x/1.2 water-immersion microscope objective (Nikon) and collected by an optical force measurement unit operating by direct detection of light-momentum changes (SensoCell, Impetux Optics). A spinning-disk confocal unit (Dragonfly, Andor) was coupled to the microscope left port. A detailed description of the setup can be found in recent publications [10, 68].

Optical trapping chambers containing primary culture cells were built in a 1.5H bottom plate (GWST-5040, Willco). Dishes were coated with a 50-µm polydimethylsiloxane (PDMS) layer, from which a 1x1 cm cavity was drawn, in which the cells were seeded as in [10]. Before the experiment, cells were gently rinsed with L15 medium three times and the cavity was filled with 50 µL of a solution containing 1-µ m diameter polystyrene beads (red fluorescent, carboxylate modified: F8816, Thermofisher, 1:2000 dilution). The microspheres were washed in L15 medium by centrifuging at 10.000 rpm for 3 minutes. Finally, the cavity was cautiously closed with a 25x25mm cover slip and mounted on the microscope.

Simultaneous optical trapping of several microbeads was performed by time-sharing the laser spot at 25 kHz. Details of the time-sharing can be found in ref. [22] This allowed for measurement of membrane tension at different sites of the neuronal axon through the extrusion of membrane nanotubes (see below). Dynamic control of the optical traps was performed with the manufacturer software (LightAce 1.6.2.0, Impetux Optics) and automated with a software development kit (SDK) in LabView (National Instruments).

4.3.1 Analysis of the time sharing dynamics of a tether microsphere

Our optical tweezers are modulated with a pair of acousto-optic deflectors to create multiple traps under a time-sharing scheme. This technique was first introduced by Visscher et al.[69] and the dynamic effect that alternating optical traps might induce onto optically trapped objects has been studied to some extent [22]. Here, we analyze the motion of a trapped bead, attached to a membrane tether, under a time-sharing regime to understand eventual artifacts. The main question here is to determine under which experimental conditions N time-shared traps from a laser beam with power P can be considered as effectively being N permanent traps with power P/N each.

We consider a microsphere that is subject to external forces from the optical trap ($F_{OT}(t) = -k_{OT}(x(t) - x_{trap})$), the medium viscosity impeding movement ($-\gamma\dot{x}(t)$) and the constant tether force due to membrane tension ($F_t(x(t)) = -F_0$). Taking $m\ddot{x}(t) \approx 0$, we first solved the microsphere equation of motion in the time-sharing scheme (Eq. 2). In the first half cycle, i.e. $0 \leq t < 40$µs and multiples thereof, during which the laser resides on trap 1, the trapping force F_{OT} is included into the equation. In the second half cycle, $40 \leq t < 80$µs and multiples thereof, there is no trapping force as the laser resides on trap 2:

$$0 = -\gamma\dot{x}(t) - k_{OT}\left(x(t) - x_{\text{trap}}\right) - F_0, \qquad 0 \leq t < 40\mu\text{s} \tag{2a}$$

$$0 = -\gamma\dot{x}(t) - F_0, \qquad 40 \leq t < 80\mu\text{s} \tag{2b}$$

Second, we solve the same equation for a continuous trap with trapping stiffness, $k_{OT}/2$:

$$0 = -\gamma\dot{x}(t) - \frac{k_{OT}}{2}\left(x(t) - x_{\text{trap}}\right) - F_0 \tag{3}$$

Once the trajectory of the bead $x(t)$ is solved, we can display the instantaneous optical force by calculating ($F(t) = -k_{OT}(x(t) - x_{trap})$) and calculate the corresponding force reading by the back focal plane force sensor through $F_i = -\frac{1}{2}k_{OT}(x(t = t_{0,i}) - x_{trap})$ where $t_{0,i}$ are the sampling instants at 33 µs in every time-shared trap. At the same time, factor 1/2 appears from the fact that there are two time-shared traps. As expected from the fact that the membrane nanotube pulls the bead back toward the cell at the time the laser spot is in trap 2, the resulting trajectory of the bead in trap 1 has a sawtooth shape (Suppl. Fig. 2).

Sampled force values at $t_{0,i}$ underestimate the permanent force The sawtooth-like trajectory of the trapped particle results in an underestimation of sampled force values, $F(t_{0,i})/2$, compared to a permanent trap with k_{OT}. Interestingly, the relative error is constant in the tethers with varying restoring forces, as shown in Suppl. Fig. 2. To experimentally decipher the effect of the described time-shared artifact in optically trapped beads, we membrane tethered a bead to a TRN axonal membrane and recorded the force measured as we created additional traps. As expected from the simulations, the force measured was reduced as one, two, and three additional traps were created. In general, the effect can be minimized by increasing the size of the trapped microsphere and strongly depends on the viscosity of the surrounding medium; e.g. it is undetectable inside cells.

4.3.2 Extrusion of membrane nanotubes and force spectroscopy

Once two beads were trapped, short contact (1s) with the axonal membrane sufficed to extrude the two lipid nanotubes (Fig. 1a). The extrusion of a nanotube translated into an increase in the force signal, which reached a peak, F_{peak}, of increasing height for a higher pulling velocity. Once the extruding bead stopped, the peak force was followed by viscoelastic relaxation, reaching a resting tension value F_{base} (Fig. 1b). The tether neck from which the membrane nanotube was extruded could slide along the axon as the optically trapped bead was moved parallel to it (Video 1), reaching a perpendicular orientation with respect to the axon to minimize the nanotube length [8]. This allowed us to separate the tether necks apart (distance d, Fig. 1c) to measure membrane tension diffusion at increasing distances along the axon.

The friction of the microbead with respect to water was calculated using the Stokes drag expression corrected for the bead-to-surface interaction ([70], Eq. 4). Heating is negligible because neurons are grown in glass, which has high thermal conductivity[71]. The approach and retraction cycles of a trapped microsphere without attachment to the neuronal membrane did not elicit cellular changes[10].

$$F_{drag} = \frac{6\pi\eta R}{1 - \frac{9R}{16h} - \frac{R^3}{8h^3}} v_{flow} \tag{4}$$

Calculating static membrane tension After extrusion of the lipid membrane tether at a given velocity, the movement of the trap was stopped and the force o the bead relaxed to a static value > 0. This value depended on the cell type, but also on the pharmacological treatment, and provides information on the mechanical coupling of the membrane to the cortex and the surface tension in the plane[3]. We calculated the effective membrane tension using the well-known relation as before, assuming a bending rigidity of $2.7{\cdot}10^{-19}$ Nm:

$$T_{base} = \frac{F_{base}^2}{8\pi^2\kappa} \tag{5}$$

When these values come from dual tether extrusion experiments, these tensions are likely underestimated by $\approx 20\%$.

4.3.3 Measuring force propagation between two tethers along the plasma membrane

The experiments involved an active trap holding a microsphere, which pulled on the corresponding nanotube at a rate of 40 µm/s, while the passive trap remained stationary. The bead was then approached back to the axon after 5 s. The membrane tension gradients originated from the active bead trap were partially diffused into the passive (Fig. 1c). As the tether force at zero velocity reads as ($f_0 = 2\pi\sqrt{(}2\kappa_B \cdot T)$) we assume that the change in membrane surface tension at the two tether necks follows Eq. 5[10, 33], from which the relative change in force on the passive trap, with respect to the active, was calculated as in Eq. 6:

$$\Delta F_{\%} = \frac{(F_{peak}^{passive}) - (F_{base}^{passive})}{(F_{peak}^{active}) - (F_{base}^{active})} \times 100 \tag{6}$$

The force transmission (Fig. 1d) reached 40% for the shortest double tether separation, $d \to 0$. To achieve this, the two beads faced each other and pulled the lipid nanotubes towards opposite directions. For increasing d, the tension rapidly dropped from the *active* to the *passive* tether, suggesting effective buffering of the membrane tension along the axon. When 20 µm apart, the tension in the passive nanotube almost vanished ($\Delta F_{\%} < 20\%$).

To calculate the extent of force propagation, we plotted the ratio of the peak force in the passive tether to the peak force in the active tether as a function of the distance between the two tethers (Figs. 2c, Suppl. Fig. 3) and fitted an exponential decay function $\exp(x) = \omega \exp(-x/\alpha)$ using weighted least squares to the absolute peak force of the passive tether.

4.4 Tension propagation model

Following Shi *et al.* [15], we augment the Stokes equation with a drag term $\frac{\eta}{k}\mathbf{v}$, which gives

$$\nabla\sigma = -\eta\nabla^2\mathbf{v} + \frac{\eta}{k}\mathbf{v}, \tag{7}$$

where σ is the tension, $\mathbf{v}$ is the velocity field of the lipid flow, η is the two-dimensional membrane viscosity, k is the Darcy permeability array of the obstacles. Assuming conservation of mass, given by

$$\frac{\partial \rho}{\partial t} + \nabla \cdot (\rho \mathbf{v}) = 0, \tag{8}$$

where ρ is the two-dimensional density of lipids. As in [15], we assume a small disturbance in the lipid density $\rho = \rho_0 + \delta\rho$ and a linear stress-strain relationship for the membrane tension $\delta\sigma = -E_0 \delta\rho/\rho_0$, E_0 represents the effective area expansion modulus of the cell membrane. This gives

$$\frac{E_0}{\eta}\nabla^2\sigma = \left(-\nabla^2 + \frac{1}{k}\right)\frac{\partial \sigma}{\partial t}. \tag{9}$$

Note that, differently from Shi *et al.* [15], we do not assume that the spacing between transmembrane obstacles is small compared to externally imposed variations in the flow field. This allows us to investigate different spatial configurations of the obstacles.

We solve Eq. (9) in COMSOL Multiphysics 6.1 using the parameters in Table 3. The pulling events were simulated by combining the definition of the tension in the tether,

$$\sigma_t = \frac{\kappa}{2r_t^2}, \tag{10}$$

with the area of the tether

$$A = 2\pi r_t l, \tag{11}$$

which gives

$$\sigma_t = \frac{2\kappa\pi^2 l^2}{A^2}. \tag{12}$$

Here, κ is the bending stiffness of the membrane, r_t is the tether radius, and l is its length. Thus, the change of the tension due to the pulling of the tether is given by

$$\frac{\mathrm{d}\sigma_t}{\mathrm{d}t} = \frac{4\kappa\pi^2 l}{A^2}\left(\frac{\mathrm{d}l}{\mathrm{d}t} - \frac{l}{A}\frac{\mathrm{d}A}{\mathrm{d}t}\right). \tag{13}$$

We take $\frac{\mathrm{d}l}{\mathrm{d}t} = v_{pull}$ and $\frac{\mathrm{d}A}{\mathrm{d}t} = \int_T k\nabla\sigma/\eta$ where T is the perimeter of the tether boundary and v_{pull} the pulling velocity. The force curves in Fig. 1 were obtained by measuring the tension at the tip of the active and passive tether. Note that we assume an initial length of the tether l_0 and did not change the geometry of the model during the simulation. Instead, we include the tension flow at the tip of the tether corresponding to Eq. 13.

Similar to the experiments, we calculated the extent of tension propagation after plotting the ratio of the peak tension in the passive tether to the peak tension in the active tether as a function of the distance between the two tethers (Figs. 2c, Suppl. Fig. 3) and fitted an exponential decay function $\exp(x) = \omega \exp(-x/\alpha)$ using weighted least squares to the peak of the passive tether.

5 Figures

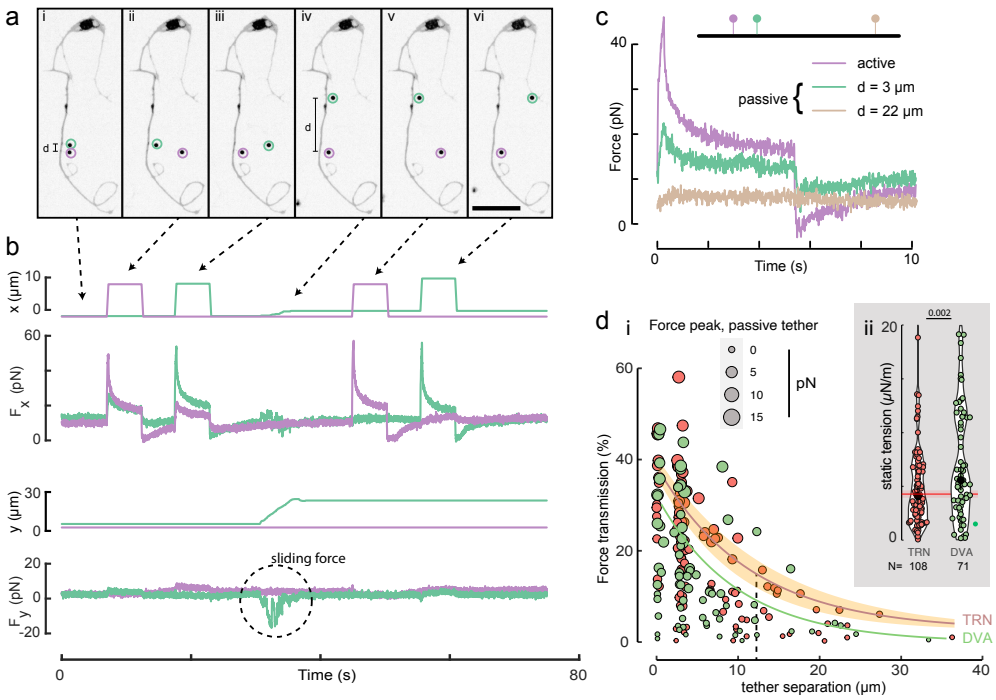

Fig. 1. A dual trap assay to measure membrane tension propagation a, Representative image of an isolated TRN with two membrane tethers extruded by two optically-trapped microspheres (purple and green circles for active and passive traps, respectively). Scalebar: 20 µm. (**i**) The two beads are connected to the axonal membrane through the extrusion of a lipid nanotube. (**ii, iii**) Both beads are sequentially pulled at 40 µm/s to a length of 10 µm (**ii**), while the resting, passive trap records changes in membrane tension at a distance d. (**iv-vi**) d is increased to record tension propagation under varying separation. **b,** X- (top) and Y- (bottom) component of the trap trajectory and force. The sequence events depicted in (a) are indicated with black arrows. The sliding friction (F_y component) between events iii and iv is indicated with a dashed circle. **c,** Simultaneous force measurement during trapezoidal pulling routines for the *active* trap and *passive* trap placed at $d = 3\mu m$ (event ii in a,b) and $d = 22\mu m$ (event v in a,b). While a small increase in membrane tension in the *passive* trap is detected when this is placed close to the active trap, membrane tension at $d = 22\mu m$ shows no force peak but a slow, second-scale tension increase. The force drop $F_x \to 0$ at $t = 5$ indicates tether buckling upon the fast approach of the trap towards the axon. Trap velocity is faster than the ability of the axon to absorb the lipidic material from the tether. Afterwards, tension homeostasis induces tension recovery.
d, Change in membrane tension measured at the *passive* lipid nanotube for increasing distances (**i**) normalized to the *active*, pulling site, calculated with Eq. 6. The size of the points corresponds to the absolute transmitted force at the passive tether. Exponential fit is weighted by the transmitted force. Red points indicate values derived from TRNs, green points from DVA. Inset shows the static membrane tension of TRN vs. DVA cultured neurons (**ii**). Median indicated as black lentil with vertical bar indicating the 95% confidence interval. Red line indicates the median of the control conditions as a reference. p-value derived from a Kruskal-Wallis test with Dunn's posthoc for pairwise comparison.

Fig. 2 ***(following page).*** **Theoretical model for tension propagation.** **a,** Schematic representation of the modeled axon: tension σ generated by pulling the active tether σ_t propagates along the axon. Left inset shows random distribution of membrane obstacles. The right inset is a snapshot of the simulation at time 2.25 s. The distance between tethers is 3 µm and the colorbar represents the tension σ. CAM, cell adhesion molecules. **b,** Top view of the membrane (a), showing possible ways to change the permeability k. **c,** Change in membrane tension measured in the *passive* lipid nanotube for increasing distances normalized to the *active*, pulling site, with different permeabilities. The size of the circle corresponds to the amount of tension in the passive tether in the simulation (small $0 < \sigma \leq 3$pN/µm, medium $3 < \sigma \leq 6$pN/µm, and big $6 < \sigma \leq 9$pN/µm). Lines are weighted exponential fits to the *passive* tether. Black represents the control condition. **d,** Lateral view of the axon showing its underlying molecular structure. Figure created in Created in BioRender. **e,** Periodic distribution of obstacles along the axon and the corresponding values of k_+ and k_-. The image on the right shows the color-coded values of k_+ (red) and k_- (blue) along the axon in the simulation. Note that the values are interpolated and follow the underlying triangular mesh. **f,** Change in membrane tension using periodic configuration for different parameters. Note that k corresponds to the mean value of the permeability along the axon that takes $k_+ = 1.5k$ and $k_- = (3k - k_+)/2$. The gray color corresponds to the control condition. **g-i,** Two-parameter sweep for the periodic condition. NaN (black squares) represents conditions for which simulations at certain displacements did not converge.

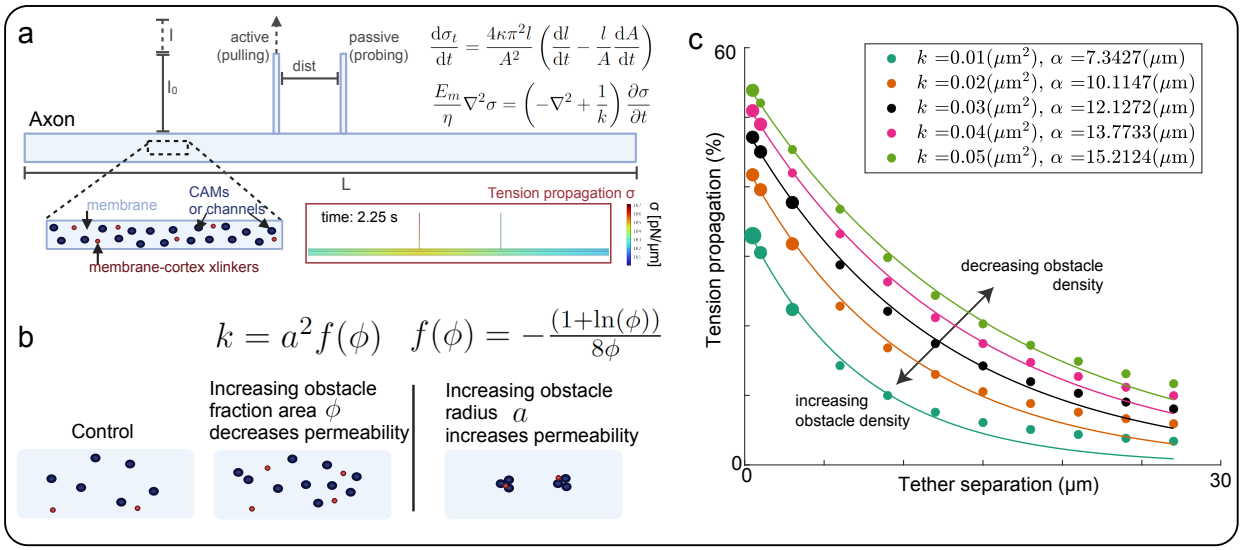
a
active (pulling)
passive (probing)
dist
Axon
L
membrane
CAMs or channels
membrane-cortex xlinkers
Tension propagation σ
time: 2.25 s
σ [pN/μm]
$\frac{d\sigma_t}{dt} = \frac{4\kappa\pi^2 l}{A^2}\left(\frac{dl}{dt} - \frac{l}{A}\frac{dA}{dt}\right)$
$\frac{E_m}{\eta}\nabla^2\sigma = \left(-\nabla^2 + \frac{1}{k}\right)\frac{\partial\sigma}{\partial t}$
b
$k = a^2 f(\phi) \quad f(\phi) = -\frac{(1+\ln(\phi))}{8\phi}$
Control
Increasing obstacle fraction area ϕ decreases permeability
Increasing obstacle radius a increases permeability
c
Tension propagation (%)
Tether separation (μm)
k =0.01(μm^2), α =7.3427(μm)
k =0.02(μm^2), α =10.1147(μm)
k =0.03(μm^2), α =12.1272(μm)
k =0.04(μm^2), α =13.7733(μm)
k =0.05(μm^2), α =15.2124(μm)
decreasing obstacle density
increasing obstacle density

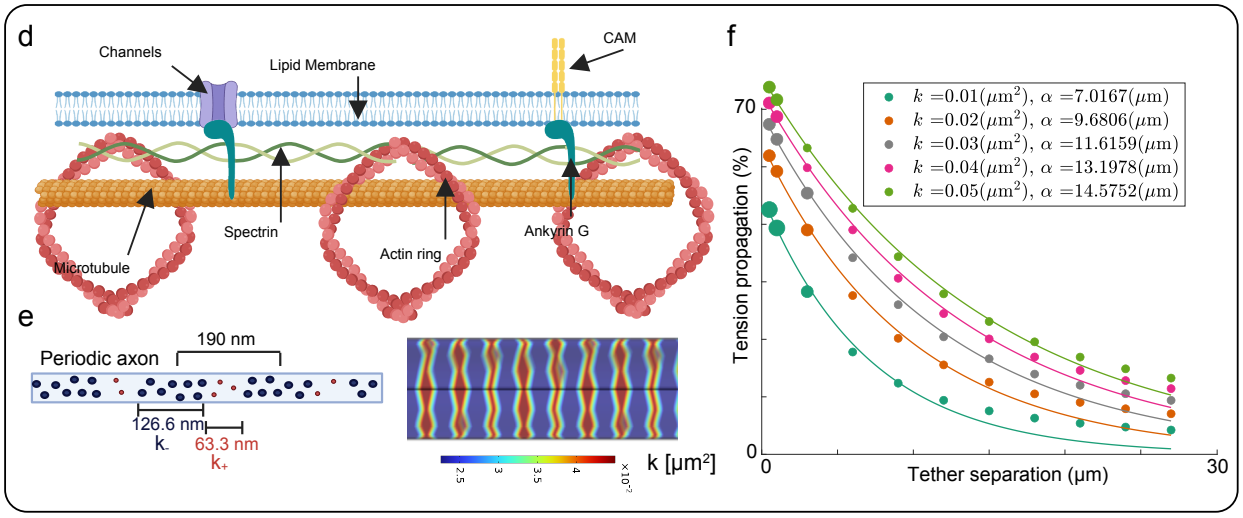
d
Channels
Lipid Membrane
CAM
Spectrin
Actin ring
Ankyrin G
Microtubule
e
Periodic axon
190 nm
126.6 nm
63.3 nm
k₋
k₊
k [μm²]
f
Tension propagation (%)
Tether separation (μm)
k =0.01(μm^2), α =7.0167(μm)
k =0.02(μm^2), α =9.6806(μm)
k =0.03(μm^2), α =11.6159(μm)
k =0.04(μm^2), α =13.1978(μm)
k =0.05(μm^2), α =14.5752(μm)

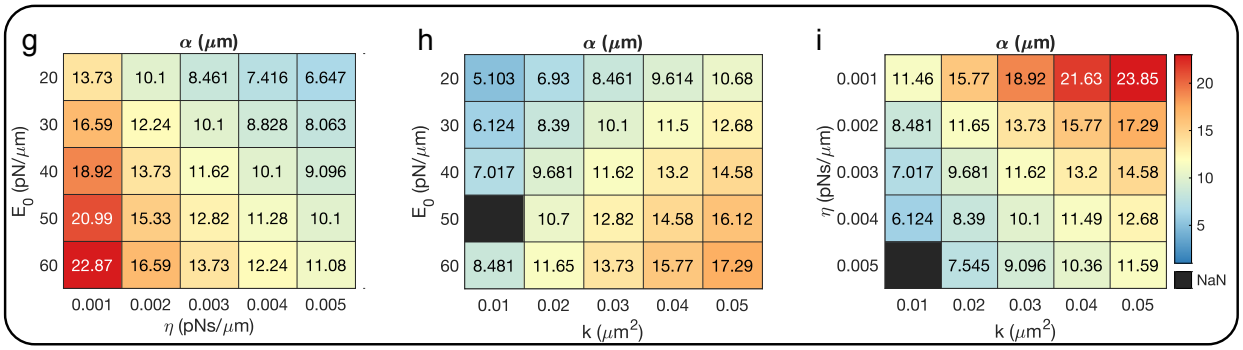
g
α (μm)
E_0 (pN/μm)
η (pNs/μm)
h
α (μm)
E_0 (pN/μm)
k (μm^2)
i
α (μm)
η (pNs/μm)
k (μm^2)
NaN

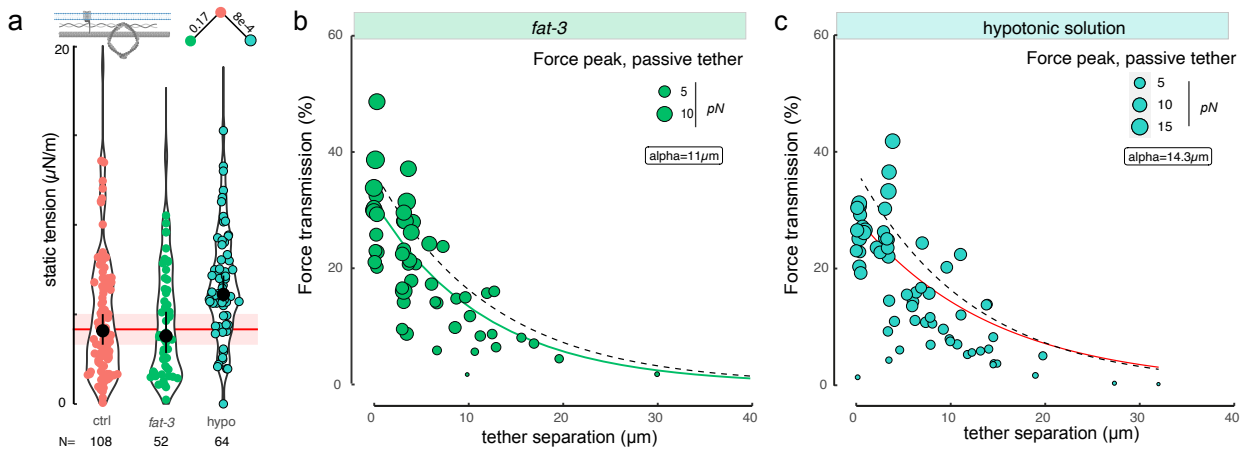

Fig. 3. Hypotonic shock but not lipid saturation modulates tether forces extruded from neurites a, Static membrane tension during the membrane extrusion for control cells, *fat-3* mutants, that perturb lipid composition, and on cells treated with hypotonic shock. Median indicated as black lentil with vertical bar indicating the 95% confidence interval. Red line indicates the median of the control conditions as a reference. N= number of measurements. Top schematic highlights membrane in skyblue. **b, c,** Tension propagation in the membrane of cells mutant for (b) *fat-3* and (c) cells treated with hypotonic solution. Solid mint (teal) line indicates a fit to the an exponential decay as described in the methods, dotted black line indicates the fit derived from control data (Fig. 1d). Size of the dots corresponds to the absolute force transmitted to the passive tether.

Fig. 4 ***(following page).*** **Tension propagation is sensitive to actin / spectrin network and microtubule integrity a,** Influence of the actin cytoskeleton on static membrane tension during the membrane extrusion from cells treated with different concentrations of cytochalasin and latrunculin to destroy actin cytoskeleton. Chronic incubation is performed over night (12h). p-values in a derived from a Kruskal-Wallis test with Dunn's posthoc for pairwise comparison. **b,** Tension propagation in cells after acute (green) and chronic (red) incubation with cytochalasin D. **c,** Simulation of tension propagation with reduced E_m and increased k compared to control, describing chronic and acute actin depolymerization. Parameters used for simulation are shown in the figure. The simulation corresponds to the periodic case. Hence, the value k is used to calculate k_+ and k_-. See also Suppl. Fig. 3. **d-f,** Influence of the microtubule cytoskeleton on (d) static membrane tension and tension propagation in the (e) *mec-12* mutant and cell treated with (f) nocodazole. **g** Influence of the spectrin cytoskeleton on static membrane tension. The images on the right show representative superresolution images of α -spectrin in wild-type and *unc-70* mutant neurons. Scalebar = 1µm. **h** Simulation of the tension propagation comparing cells with periodic (black, dotted) and random (green, solid line) obstacle arrangement. **i** Tension propagation in *unc-70* mutant cells. For all panels (a, d, g): The top schematic highlights different cytoskeleton elements of interest. The median is indicated as black lentil with a vertical bar indicating the confidence interval 95%. The red line indicates the median of the control conditions as a reference. N = number of measurements. For panels displayed in b, e, f and i: solid lines indicate a fit to an exponential decay as described in the methods, dotted black line indicates the fit derived from control data (Fig. 1d). The size of the dots corresponds to the absolute force transmitted to the passive tether.

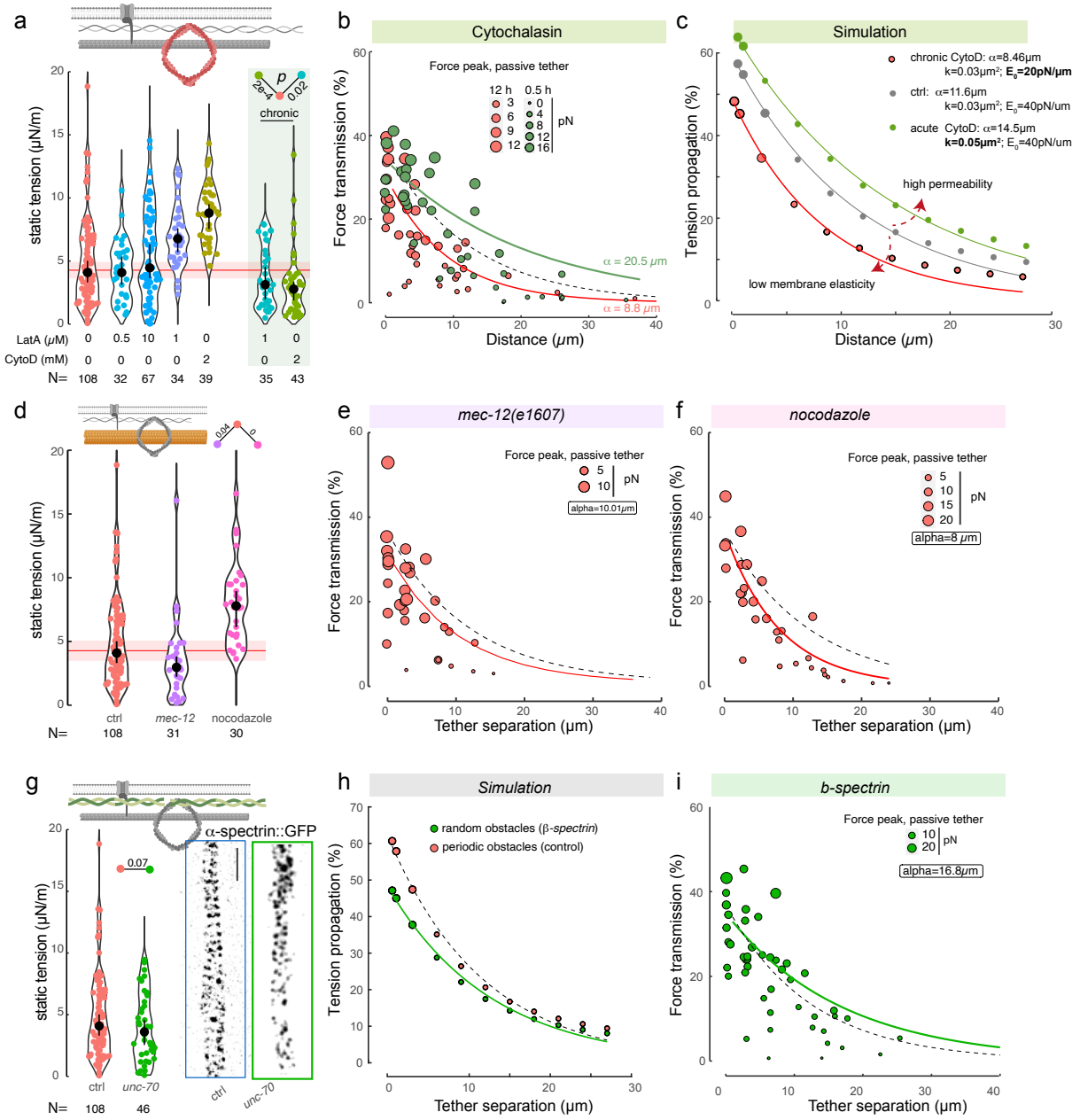
a
static tension (μN/m)
p
2e-4
0.02
chronic
LatA (μM) 0 0.5 10 1 0 1 0
CytoD (mM) 0 0 0 0 2 0 2
N= 108 32 67 34 39 35 43
b
Cytochalasin
Force peak, passive tether
12 h 0.5 h
3 0
6 4
9 8
12 12
16
pN
α = 20.5 μm
α = 8.8 μm
Force transmission (%)
Distance (μm)
c
Simulation
chronic CytoD: α=8.46μm
k=0.03μm²; E0=20pN/μm
ctrl: α=11.6μm
k=0.03μm²; E0=40pN/um
acute CytoD: α=14.5μm
k=0.05μm²; E0=40pN/um
high permeability
low membrane elasticity
Tension propagation (%)
Distance (μm)
d
static tension (μN/m)
0.04
0
ctrl
mec-12
nocodazole
N= 108 31 30
e
mec-12(e1607)
Force peak, passive tether
5
10
pN
alpha=10.01μm
Force transmission (%)
Tether separation (μm)
f
nocodazole
Force peak, passive tether
5
10
15
20
pN
alpha=8 μm
Force transmission (%)
Tether separation (μm)
g
α-spectrin::GFP
static tension (μN/m)
0.07
ctrl
unc-70
N= 108 46
ctrl
unc-70
h
Simulation
random obstacles (β-spectrin)
periodic obstacles (control)
Tension propagation (%)
Tether separation (μm)
i
b-spectrin
Force peak, passive tether
10
20
pN
alpha=16.8μm
Force transmission (%)
Tether separation (μm)

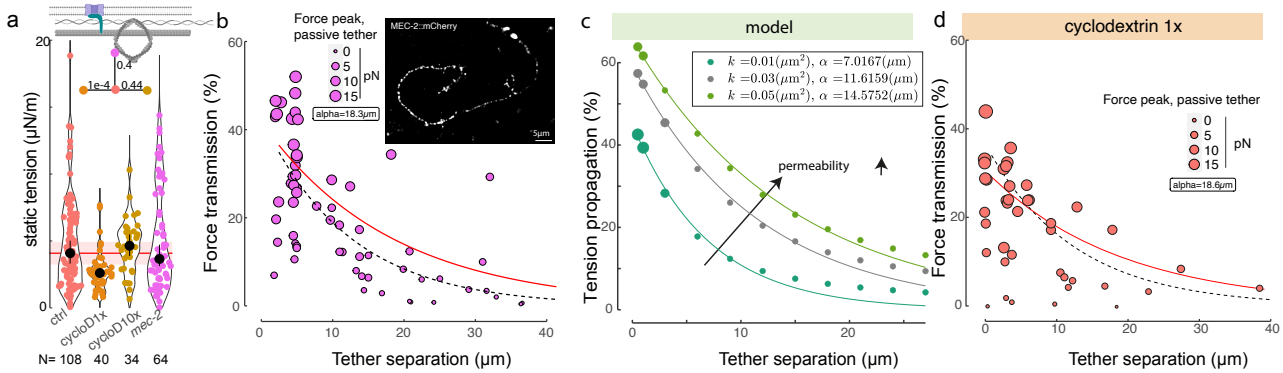

Fig. 5. Membrane condensation of MEC-2 delimits tension propagation along the membrane
a, Static tension during the membrane extrusion from cells mutant for *mec-2* or treated with increasing concentrations of Cyclodextrin (cycloD; 1x or 10x, see Methods). Top schematic highlights channel-cytoskeleton crosslinkers in blue. Median indicated as black lentil with vertical bar indicating the 95% confidence interval. Red line indicates the median of the control conditions as a reference. N=number of measurements. p-value derived from a Kruskal-Wallis test with Dunn's posthoc for pairwise comparison. **b,** Force propagation between active and passive tether for *mec-2* mutant neurons. Inset: density of MEC-2 along the axon in cultured neurons as a proxy for membrane obstacles. Solid red line indicates a fit to the an exponential decay as described in the methods, dotted black line indicates the fit derived from control data (Fig. 1d). Size of the dots corresponds to the absolute force transmitted to the passive tether. **c,** Simulation of the tension propagation comparing cells with decreasing obstacle density; increasing permeability k. The simulation corresponds to the periodic case. Hence, the value k is used to calculate k_+ and k_-. **d,** Tension propagation for neurons treated with cyclodextrin to sequester cholesterol. On top, representative confocal image of an isolated TRN with mCherry-labeled MEC-2 protein distributed in punctate fashion.

6 Supplementary Material

6.1 Suppl. Figures

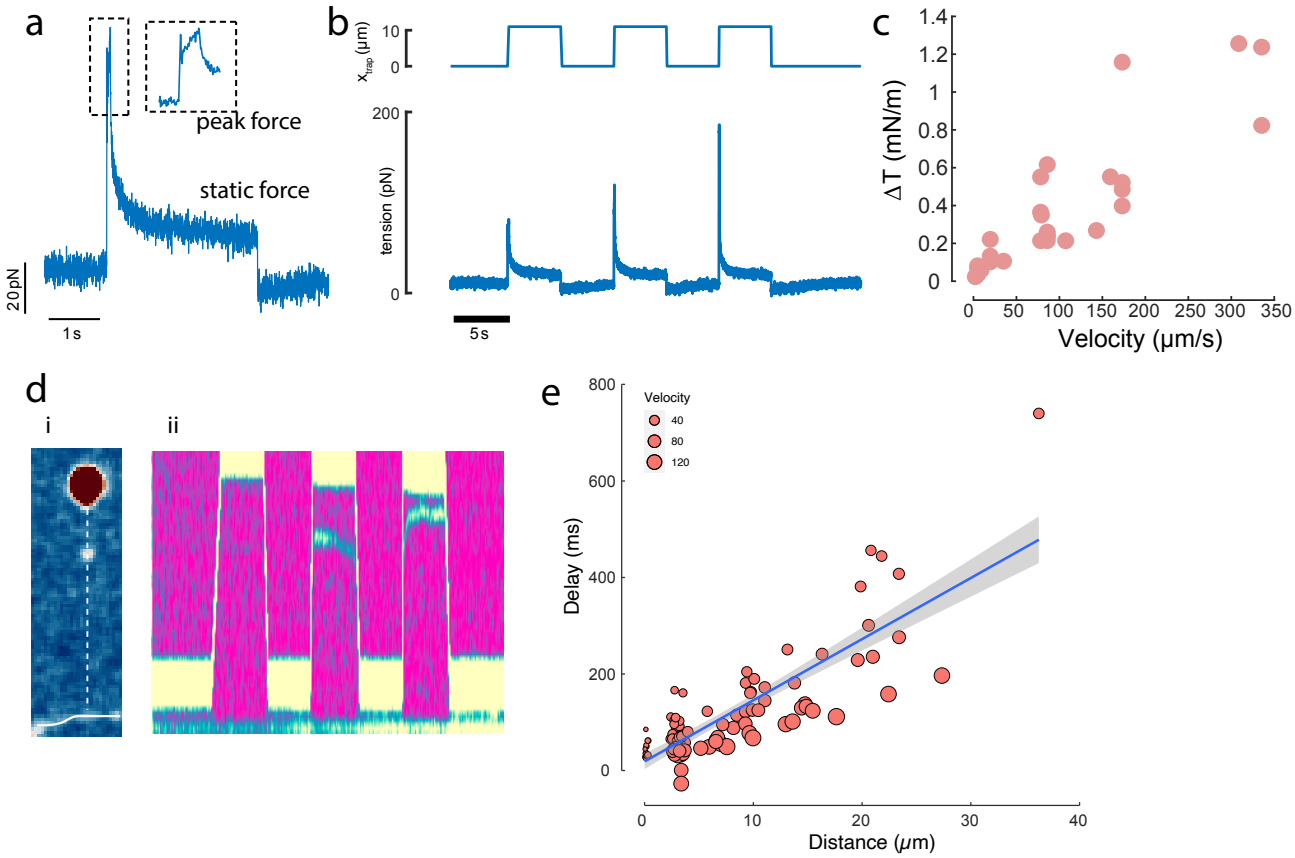

Suppl. Fig. 1. Tether extrusion dynamics **a,** Tether force profile upon extrusion. Inset shows the force peak during the extrusion event. Once the trap stops moving, force decays to a static value, indicative for the resting membrane tension. **b,** Consecutive tether extrusion events at increasing velocity. **c,** Peak membrane tension vs extrusion velocity. The slope is proportional to the viscosity. **d,** Representative plot of the RPI. (i) shows a snapshot of the bead tethered to the membrane. The tether is invisible but highlighted with a dotted line. The spherical protrusion travels toward the cell. (ii) Kymograph, taken on the dotted line in the image above, shows the three consecutive extrusion events and the traveling RPI along the tether. **e,** Plot of the delay between the two force peaks and the tether separation distance. Size of the dots corresponds to the velocity (µm/s). Blue line is the linear regression with the shadow as the 95% confidence interval.

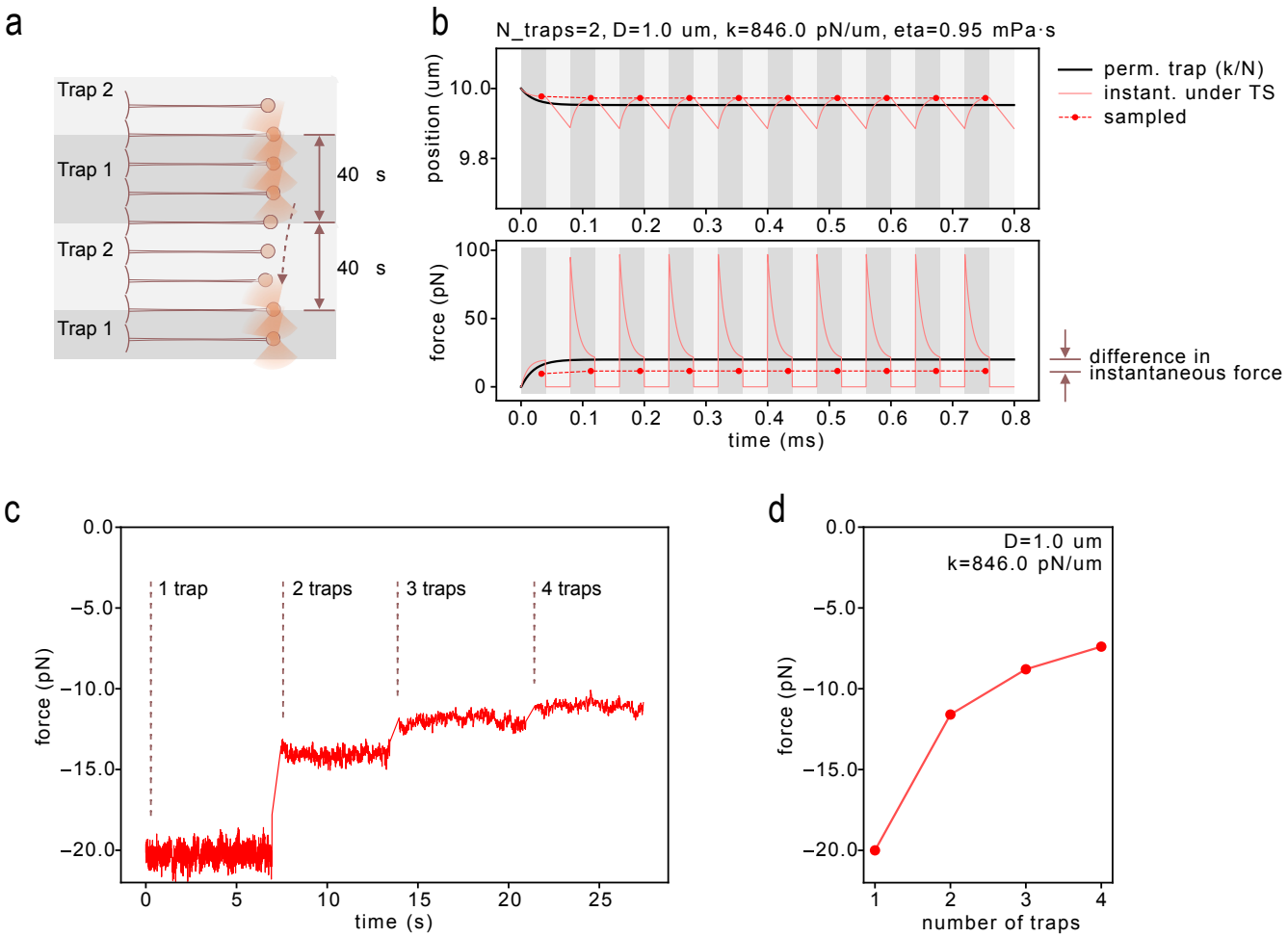

Suppl. Fig. 2. Evaluating multiple trap time sharing dynamics. **a,** Sequence onto one of the two optically-trapped beads tethered to the axonal membrane in a dual time-shared trap configuration at a frequency of f_{TS}=25 kHz (period $1/f_{TS}$=40 µs). During the active period (dark shadowed), trap 1 holds the bead and measures a force datum at t=33 µs. During the passive period (light shadow) the laser resides in trap 2, tethering force on bead 1 is not optically balanced, hence producing a slight bead creep towards the axon. **b,** Simulation of the instantaneous trajectory (top) and force (bottom) acting onto the bead for a tether applying a constant force of 20 pN. Instantaneous trajectory is plotted in pink, sampled values at 25/2=12.5 kHz are represented by red dots connected by dashed lines. In black, the instantaneous trajectory resulting from a permanent trap with stiffness 846/2=423 pN/µm is shown. (See methods for details). **c,** Force measurement on an optically-trapped bead membrane-tethered to the axon under a sequence of increasing number of traps. Only trap 1 is tethered to the membrane with 20 pN. Force underestimation appears when additional traps are created away from the trap. **d,** Simulation of the time-sharing effect on N_{traps}=1, 2, 3, and 4 connected to stiff membrane tethers.

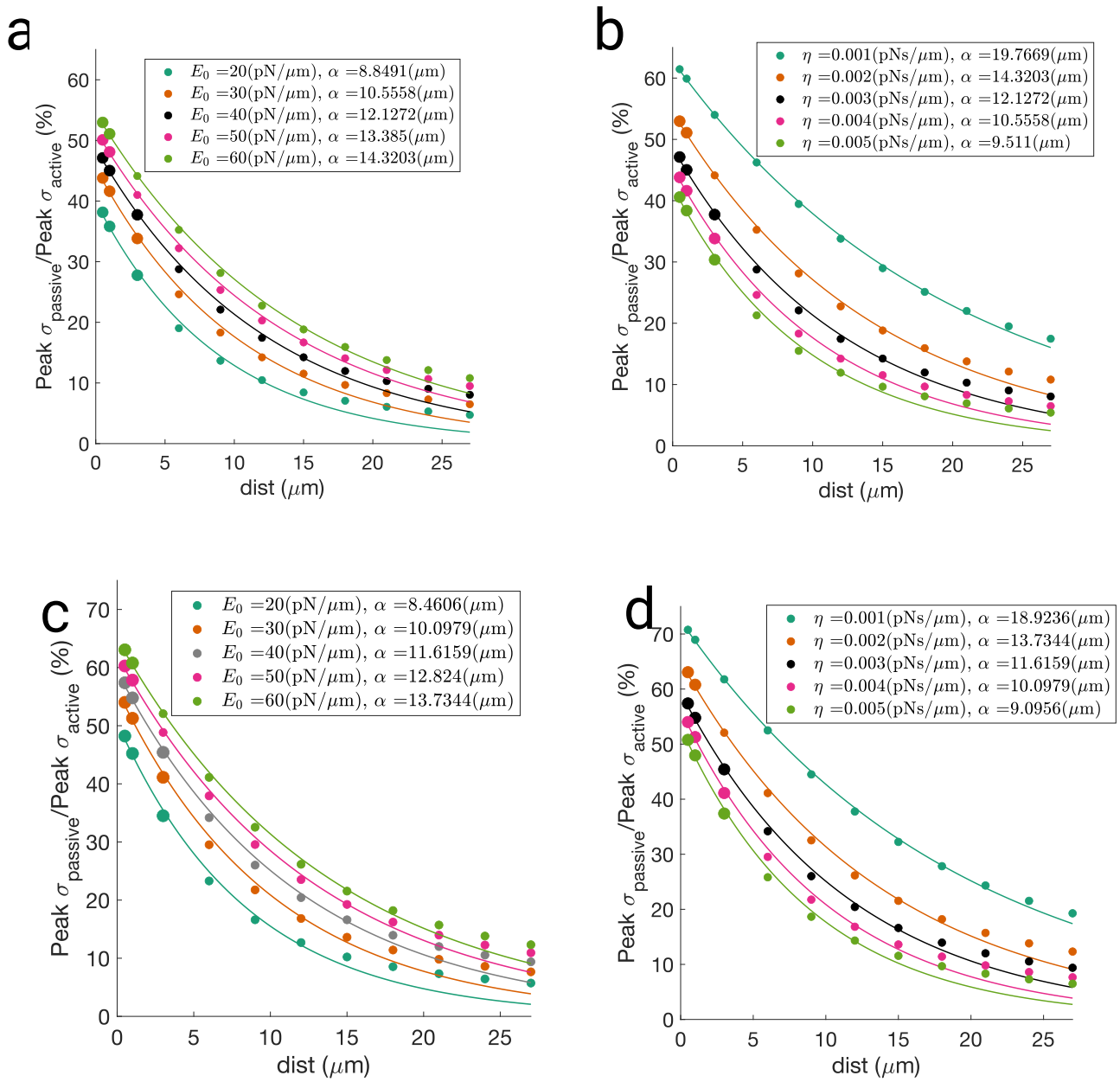

Suppl. Fig. 3. Theoretical model for tension propagation. a, b, Change in membrane tension measured at the *passive* lipid nanotube for increasing distances normalized to the *active*, pulling site, with different (a) membrane expansion modulus and (b) viscosities. Circle size corresponds to the amount of tension in the passive tether in the simulation (small $0 < \sigma \leq 3$pN/µm, medium $3 < \sigma \leq 6$pN/µm, and big $6 < \sigma \leq 9$pN/µm). Lines are weighted exponential fits to the *passive* tether. Black color represents the control condition. **c, d,** Change in membrane tension propagation using the periodic configuration for different parameters (c) membrane expansion modulus and (d) viscosities. Note that k corresponds to the mean value of the permeability along the axon taking $k_+ = 1.5k$ and $k_- = (3k - k_+)/2$. Grey color corresponds to the control condition.

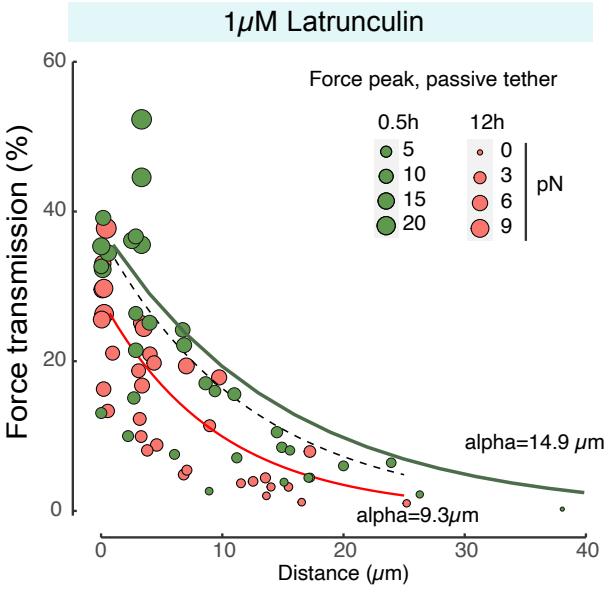

Suppl. Fig. 4. Tension propagation with different LatA concentrations. Change in membrane tension measured at the *passive* lipid nanotube for increasing distances normalized to the *active*, pulling site, with different incubation times of Latrunculin A. The size of the points corresponds to the absolute transmitted force at the passive tether. Exponential fit is weighted by the transmitted force, α indicates extent of tension propagation. Red points indicate values derived from over night incubation, green points from 30 min incubation with 1 μM LatA.

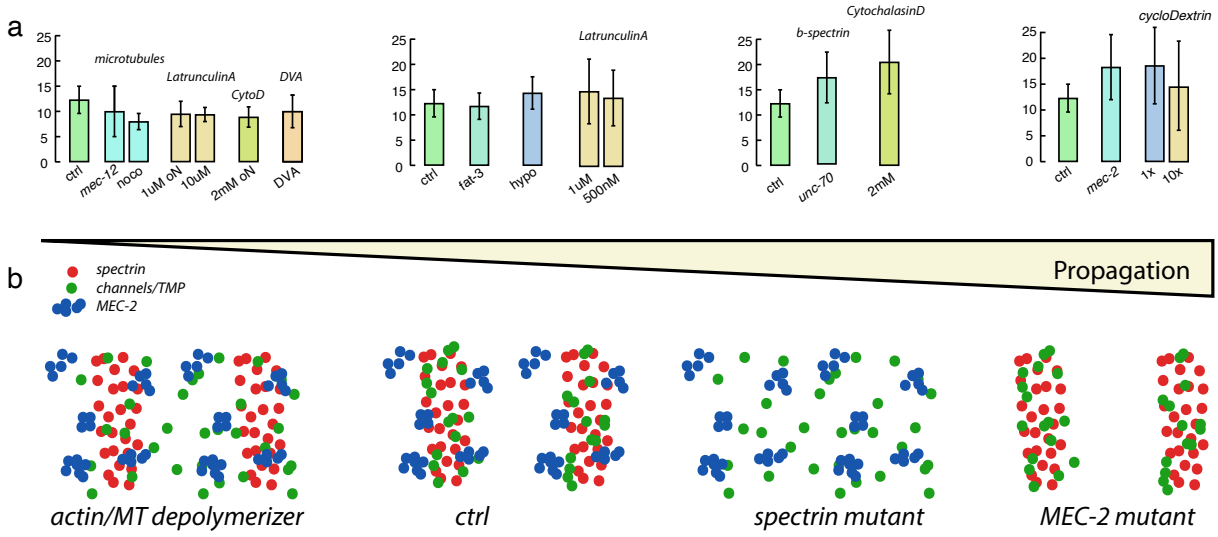

Suppl. Fig. 5. Summary of the treatments changing tension propagation a, Fit parameters derived from the tension propagation measurement under the described perturbation. **b,** Schematic of the outcome on the arrangement of obstacles impeding tension propagation. Different mechanism can lead to the same outcome, e.g. removal of the periodic arrangement as well as obstacle clustering.

6.2 Supplementary Videos

Video 1. Double-tether extrusion experiment to probe tension propagation

Representative video of an isolated touch receptor neuron with two membrane-attached microspheres. First, the two spheres were extruded consecutively while monitoring tension propagation to the static probe. The same protocol was repeated at a varying distance to yield the result as shown in Fig. 1.

Video 2. Pearling instability in extruded tethers

Three consecutive extrusion events with increasing velocity. Note that the pearling is visible during the third pull at the highest velocity and the largest tension gradient. For scale, the microsphere is d=1µm, and the frame rate is 10 Hz.

Video 3. Video of in silico tension propagation

Simulation of tension propagation between the active tether (left) and the passive tether using the assumption of periodic arranged obstacles.

6.3 Supplementary Tables

Fit parameters derived from the experimental data

Table 1. Fit parameters derived from the experimental data

	tension propagation		static tension			
	δ±SE	y_0±SE	σ±SD (10^-6 N/m)	p(tension)	Cohen's D	df
nocodazole	8±1.6	36.5±2.1	8±3.1	0	0.44	28
cytoD ON	8.9±2	30±1.7	3.1±2.5	0.0002	0.63	41
LatAoN	9.55±2.5	28±1.66	3.7±2.4	0.02	0.48	33
LatA 10uM	9.4±1.4	35±1.4	5.9±4.5	0.19	0	65
DVA	9.8±3.8	31±2.2	8.4±6.6	0.002	0.4	69
Mec-12	10±5	31±2.5	5±6.6	0.035	0.14	29
fat	11.7±2.6	31±1.6	4.5±3	0.17	0.29	50
WT	**12.3±2.7**	**36.9±1.9**	**5.9±6.1**			**106**
latA 500nM	13.6±5.5	35±2.5	4.8±4.3	0.25	0.21	30
latA 1uM	14.9±6.4	38±3	7.55±4.2	0.0004	0.31	32
hypotonic	14.3±3.2	28.8±1.4	6.6±3	0.0008	0.14	62
cyclodex-10mM	14.6±8.3	32±2.9	4.6±2	0.44	0.29	32
spectrin	16.8±4.9	34±2	4.7±5	0.07	0.22	44
MEC-2	18.3±6.3	37±2.4	5.5±4.3	0.4	0.07	62
Cyclodex-low	18.6±7.4	30.7±1.9	2.8±1.5	0.0001	0.71	38
cytoD 2uM	20.5±6.3	34.4±2	9.1±3	0	0.67	37

C. elegans strains used in this study

Table 2. Strains used in this study

Strains	Genotype	Source	Used in Fig.
N2 Bristol	N2	CGC (*)	Fig 1
GN692	ljSi1[*mec-7*p:GCaMP6s::SL2::tagRFP] II; *lite-1*(ce314)	[72]	Fig. 1
MSB1099	*fat-3*(wa22) IV; ljSi1 [*mec-7*p:GCaMP6s::SL2::tagRFP] II	this study;[31]	Fig. 3
GOU3103	*unc-70*(cas962[GFP::*unc-70*] V	[73]	
MSB1176	uIs31(*mec-17*::GFP);oxIs95(*pdi-2*p::*unc-70*;*myo-2*p::GFP); *unc-70*(s1502)	[30]	Fig. 4
GN510	*mec-4*(zdIs5) I; *mec-12*(e1607) III	[25]	Fig.4
MSB537	ljSi1(*mec-7*p:GCaMP6s::SL2::tagRFP) II;*lite-1*(ce314);*mec-2*(mir8(W119STOP))	[74]	Fig.5
MSB273	mirIs19[*nlp-12*p::GAL-4;*unc-122*p::mCherry]; syIs423 [15xUAS::Δ*pes-10*::GCaMP6s::SL2::mKate2::let-858 3'UTR;*myo-2*p::NLS::mCherry + 1kb DNA ladder(NEB)]	[10]	Fig.1

6.3.1 Parameter choice in the tension propagation model

Table 3. Tension propagation model parameters

Symbol	value	units	description	reference
L	190	µm	axon length	-
r	100	nm	axon radius	-
c_{t1}	55	µm	center of the active tether	-
κ	1.19×10^{-19}	J	bending stiffness of the membrane	[15]
σ_0	180	pN/µm	initial tension	-
r_0	$\sqrt{\kappa/(2\sigma_0)}$	µm	initial tether radius	[15]
Δ_t	0.005	s	time step	-
t_{end}	12	s	final time	-
l_0	1	µm	initial tether length	exp. data
l_{max}	11	µm	maximal tether length	exp. data
$t_{p_{ini}}$	2	s	start time of active pulling	-
$t_{p_{end}}$	$t_{p_{ini}}$ + 5s	s	end time of active pulling	exp. data
v_{pull}	40	µm/s	pulling velocity	exp. data
k	3×10^{-2}	µm^2	Darcy permeability	[15]
η	3×10^{-3}	pN s/µm	membrane viscosity	[15]
E_0	40	pN/µm	effective area expansion modulus of the cell membrane	[15]

References

[1] Ghisleni, A., Gauthier, N. C., Mechanotransduction through membrane tension: It's all about propagation? (2024).

[2] Roux, A. L. L., Quiroga, X., Walani, N., Arroyo, M., Roca-Cusachs, P., The plasma membrane as a mechanochemical transducer. *Philosophical Transactions of the Royal Society B: Biological Sciences* **374** (2019).

[3] Diz-Muñoz, A., et al., Control of directed cell migration in vivo by membrane-to-cortex attachment. *PLoS Biology* **8**, e1000544 (2010).

[4] Sukharev, S., Sachs, F., Molecular force transduction by ion channels: diversity and unifying principles. *Journal of Cell Science* **125**, 3075–3083 (2012).

[5] Appadurai, D., et al., Plasma membrane tension regulates eisosome structure and function. *Molecular Biology of the Cell* **31**, 287–303 (2020).

[6] Dai, J., Sheetz, M. P., Cell membrane mechanics.

[7] Raucher, D., Sheetz, M. P., Characteristics of a membrane reservoir buffering membrane tension. *Biophys J* **77**, 1992–2002 (1999).

[8] Datar, A., Bornschlögl, T., Bassereau, P., Prost, J., Pullarkat, P. A., Dynamics of membrane tethers reveal novel aspects of cytoskeleton-membrane interactions in axons. *Biophysical Journal* **108**, 489–497 (2015).

[9] Brownell, W. E., Qian, F., Anvari, B., Cell membrane tethers generate mechanical force in response to electrical stimulation. *Biophysical Journal* **99**, 845–852 (2010).

[10] Das, R., et al., An asymmetric mechanical code ciphers curvature-dependent proprioceptor activity. *Science Advances* **7**, 1–20 (2021).

[11] Pradhan, S., Williams, M. A., Hale, T. K., Changes in the properties of membrane tethers in response to hp1α depletion in mcf7 cells. *Biochemical and Biophysical Research Communications* **587**, 126–130 (2022).

[12] Dai, J., Sheetz, M. P., Wan, X., Morris, C. E., Membrane tension in swelling and shrinking molluscan neurons. *J Neurosci* **18**, 6681–6692 (1998).

[13] Rangamani, P., The many faces of membrane tension: Challenges across systems and scales. *Biochimica et Biophysica Acta - Biomembranes* **1864** (2022).

[14] Mashanov, G. I., et al., Heterogeneity of cell membrane structure studied by single molecule tracking. *Faraday Discussions* **232**, 358–374 (2021).

[15] Shi, Z., Graber, Z. T., Baumgart, T., Stone, H. A., Cohen, A. E., Cell membranes resist flow. *Cell* **175**, 1769–1779.e13 (2018).

[16] Rangamani, P., Mandadap, K. K., Oster, G., Protein-induced membrane curvature alters local membrane tension. *Biophysical Journal* **107**, 751–762 (2014).

[17] Belly, H. D., et al., Cell protrusions and contractions generate long-range membrane tension propagation. *Cell* **186**, 3049–3061.e15 (2023).

[18] Shi, Z., Innes-Gold, S., Cohen, A. E., Membrane tension propagation couples axon growth and collateral branching. *Science Advances* **8** (2022).

[19] Perez, C. G., et al., Rapid propagation of membrane tension at a presynaptic terminal. *Science Advances* **4411**, 2021.05.26.445801 (2022).

[20] Jauffred, L., Callisen, T. H., Oddershede, L. B., Visco-elastic membrane tethers extracted from escherichia coli by optical tweezers. *Biophys J* **93**, 4068–4075 (2007).

[21] Guilford, W. H., Tournas, J. A., Dascalu, D., Watson, D. S., Creating multiple time-shared laser traps with simultaneous displacement detection using digital signal processing hardware. *Analytical Biochemistry* **326**, 153–166 (2004).

[22] Català-Castro, F., et al., Measuring age-dependent viscoelasticity of organelles, cells and organisms with time-shared optical tweezer microrheology. *Nature Nanotechnology* (2025).

[23] Sanzeni, A., et al., Somatosensory neurons integrate the geometry of skin deformation and mechanotransduction channels to shape touch sensing. *eLife* **8**, 1–44 (2019).

[24] Krieg, M., Dunn, A. R., Goodman, M. B., Mechanical systems biology of c. elegans touch sensation. *BioEssays* **37**, 335–344 (2015).

[25] Krieg, M., et al., Genetic defects in β-spectrin and tau sensitize c. elegans axons to movement-induced damage via torque-tension coupling. *eLife* **6**, e20172 (2017).

[26] Das, A., et al., Article c . elegans touch receptor neurons direct mechanosensory complex organization via repurposing conserved basal lamina proteins article c . elegans touch receptor neurons direct mechanosensory complex organization via repurposing conserved basal lam. *Current Biology* 1–19 (2024).

[27] Cueva, J. G., Mulholland, A., Goodman, M. B., Nanoscale organization of the mec-4 deg/enac sensory mechanotransduction channel in caenorhabditis elegans touch receptor neurons. *Journal of Neuroscience* **27**, 14089–14098 (2007).

[28] Sanfeliu-Cerdán, N., Lin, L.-C., Dunn, A. R., Goodman, M. B., Krieg, M., Visualizing neurons under tension in vivo with optogenetic molecular force sensors. *Methods in molecular biology (Clifton, N.J.)* **2600**, 239–266 (2023).

[29] O'Hagan, R., Chalfie, M., Goodman, M. B., The mec-4 deg/enac channel of caenorhabditis elegans touch receptor neurons transduces mechanical signals. *Nature Neuroscience* **8**, 43–50 (2005).

[30] Krieg, M., Dunn, A. R., Goodman, M. B., Mechanical control of the sense of touch by β-spectrin. *Nature Cell Biology* **16**, 224–233 (2014).

[31] Vásquez, V., Krieg, M., Lockhead, D., Goodman, M. B., Phospholipids that contain polyunsaturated fatty acids enhance neuronal cell mechanics and touch sensation. *Cell Reports* **6**, 70–80 (2014).

[32] Bussell, S. J., Koch, D. L., Hammer, D. A., Effect of hydrodynamic interactions on the diffusion of integral membrane proteins: diffusion in plasma membranes. *Biophysical Journal* **68**, 1836–1849 (1995).

[33] Hochmuth, R. M., Shao, J. Y., Dai, J., Sheetz, M. P., Deformation and flow of membrane into tethers extracted from neuronal growth cones. *Biophys J* **70**, 358–369 (1996).

[34] Li, Z., et al., Membrane tether formation from outer hair cells with optical tweezers. *Biophys J* **82**, 1386–1395 (2002).

[35] Krieg, M., Helenius, J., Heisenberg, C. P., Muller, D. J., A bond for a lifetime: Employing membrane nanotubes from living cells to determine receptor-ligand kinetics. *Angewandte Chemie - International Edition* **47**, 9775–9777 (2008).

[36] Bar-Ziv, R., Moses, E., Instability and "pearling" states produced in tubular membranes by competition of curvature and tension. *Physical Review Letters* **73**, 1392–1395 (1994).

[37] Boedec, G., Jaeger, M., Leonetti, M., Pearling instability of a cylindrical vesicle. *Journal of Fluid Mechanics* **743**, 262–279 (2014).

[38] Li, W., Feng, Z., Sternberg, P. W., A c. elegans stretch receptor neuron revealed by a mechanosensitive trp channel homologue. *Nature* **440**, 684–687 (2006).

[39] Xu, K., Zhong, G., Zhuang, X., Actin, spectrin, and associated proteins form a periodic cytoskeletal structure in axons. *Science (New York, NY)* **339**, 452–456 (2013).

[40] D'Este, E., Kamin, D., Göttfert, F., El-Hady, A., Hell, S. W., Sted nanoscopy reveals the ubiquity of subcortical cytoskeleton periodicity in living neurons. *Cell Reports* **10**, 1246–1251 (2015).

[41] Kahn-Kirby, A. H., et al., Specific polyunsaturated fatty acids drive trpv-dependent sensory signaling in vivo. *Cell* **119**, 889–900 (2004).

[42] Else, P. L., The highly unnatural fatty acid profile of cells in culture (2020).

[43] Dharan, R., et al., Intracellular pressure controls the propagation of tension in crumpled cell membranes. *Nature Communications* **16**, 91 (2025).

[44] Rentsch, J., et al., Sub-membrane actin rings compartmentalize the plasma membrane. *Journal of Cell Biology* **223** (2024).

[45] Spector, I., Shochet, N., Kashman, Y., Groweiss, A., Latrunculins: Novel marine toxins that disrupt microfilament organization in cultured cells. *Science* **219**, 493–495 (1983).

[46] Schliwa, M., Action of cytochalasin d on cytoskeletal networks. *Journal Cell Biology* **92**, 79–1 (1982).

[47] Qu, Y., Hahn, I., Webb, S. E., Pearce, S. P., Prokop, A., Periodic actin structures in neuronal axons are required to maintain microtubules. *Molecular Biology of the Cell* **28**, 296–308 (2017).

[48] Stevenson, B. R., Begg, D. A., Concentration-dependent effects of cytochalasin d on tight junctions and actin filaments in mdck epithelial cells. *Journal of cell science* 367–375 (1994).

[49] Chalfie, M., Thomson, J. N., Structural and functional diversity in the neuronal microtubules of caenorhabditis elegans. *The Journal of Cell Biology* **93**, 15–23 (1982).

[50] Lockhead, D., et al., The tubulin repertoire of c. elegans sensory neurons and its context-dependent role in process outgrowth. *Molecular biology of the cell* **27**, 3717–3728 (2016).

[51] Chalfie, M., Au, M., Genetic control of differentiation of the caenorhabditis elegans touch receptor neurons. *Science (New York, N.Y.)* **243**, 1027–33 (1989).

[52] Solinger, J. A., et al., The caenorhabditis elegans elongator complex regulates neuronal α-tubulin acetylation. *PLoS Genetics* **6** (2010).

[53] He, L., et al., Cortical anchoring of the microtubule cytoskeleton is essential for neuron polarity. *eLife* **9**, 1–32 (2020).

[54] Bennett, J. S., et al., Spatially-resolved rotational microrheology with an optically-trapped sphere. *Scientific Reports* **3**, 1–5 (2013).

[55] Malaiwong, N., et al., Mechanical load conditions the spectrin network to 'runon' proteolysis and promotes early onset neurodegeneration. *BioRxiv* (2024).

[56] Ghisleni, A., Bonilla-Quintana, M., Crestani, M., Rangamani, P., Gauthier, N. C., Mechanically induced conformational transition of spectrin in the mammalian cell cortex. *Nature Communications* **122**, 263a (2024).

[57] Wernert, F., et al., The actin-spectrin submembrane scaffold restricts endocytosis along proximal axons. *Science (New York, N.Y.)* **385**, eado2032 (2024).

[58] Qi, Y., et al., Membrane stiffening by stoml3 facilitates mechanosensation in sensory neurons. *Nature Communications* **6**, 8512 (2015).

[59] Huber, T. B., et al., Podocin and mec-2 bind cholesterol to regulate the activity of associated ion channels. *Proceedings of the National Academy of Sciences of the United States of America* **103**, 17079–17086 (2006).

[60] Brown, A. L., Liao, Z., Goodman, M. B., Mec-2 and mec-6 in the caenorhabditis elegans sensory mechanotransduction complex: Auxiliary subunits that enable channel activity. *Journal of General Physiology* **131**, 605–616 (2008).

[61] Needham, D., Nunn, R. S., Elastic deformation and failure of lipid bilayer membranes containing cholesterol. *Biophysical Journal* **58**, 997–1009 (1990).

[62] Hochmuth, R. M., Micropipette aspiration of living cells. *Journal of Biomechanics* **33**, 15–22 (2000).

[63] Echarri, A., Pozo, M. A. D., Caveolae - mechanosensitive membrane invaginations linked to actin filaments (2015).

[64] Taylor, S. R., et al., Molecular topography of an entire nervous system. *Cell* **184**, 1–19 (2021).

[65] Yang, Q., Liu, J., Wang, Z., 4.1n-mediated interactions and functions in nerve system and cancer (2021).

[66] Stiernagle, T., Maintenance of c. elegans. *WormBook : the online review of C. elegans biology* 1–11 (2006).

[67] de-la Riva, M. P., Fontrodona, L., Villanueva, A., Cerón, J., Basic caenorhabditis elegans methods: Synchronization and observation. *Journal of Visualized Experiments* e4019 (2012).

[68] Català-Castro, F., Venturini, V., Ortiz-Vásquez, S., Ruprecht, V., Krieg, M., Direct force measurements of subcellular mechanics in confinement using optical tweezers. *Journal of Visualized Experiments* **2021**, 1–35 (2021).

[69] Visscher, K., Gross, S. P., Block, S. M., Construction of multiple-beam optical traps with nanometer-resolution position sensing. *IEEE Journal on Selected Topics in Quantum Electronics* **2**, 1066–1076 (1996).

[70] Schäffer, E., Nørrelykke, S. F., Howard, J., Surface forces and drag coefficients of microspheres near a plane surface measured with optical tweezers. *Langmuir* **23**, 3654–3665 (2007).

[71] Català, F., Marsà, F., Montes-Usategui, M., Farré, A., Martín-Badosa, E., Extending calibration-free force measurements to optically-trapped rod-shaped samples. *Scientific Reports* **7**, 1–10 (2017).

[72] Nekimken, A. L., et al., Pneumatic stimulation of c. elegans mechanoreceptor neurons in a microfluidic trap. *Lab Chip* **17**, 1116–1127 (2017).

[73] Jia, R., et al., Spectrin-based membrane skeleton supports ciliogenesis. *PLOS Biology* **17**, e3000369 (2019).

[74] Sanfeliu-Cerdán, N., et al., A mec-2/stomatin condensate liquid-to-solid phase transition controls neuronal mechanotransduction during touch sensing. *Nature Cell Biology* **25**, 1590–1599 (2023).